# P1.18 AN EVALUATION OF CLOUD MICROPHYSICS SCHEMES IN A MESOSCALE MODEL USING MICROWAVE MEASUREMENTS

Mei Han[*,1,2], Scott A. Braun[2], William S. Olson[2,3], P. Ola G. Persson[4,5], Jian-Wen Bao[5]

[1]Goddard Earth Sciences and Technology Center, University of Maryland at Baltimore County, Baltimore, Maryland
[2]Laboratory for Atmospheres, NASA Goddard Space Flight Center, Greenbelt, Maryland
[3]Joint Center for Earth Systems Technology, University of Maryland at Baltimore County, Baltimore, Maryland
[4]Cooperative Institute for Research in Environmental Sciences, University of Colorado, Boulder, Colorado
[5]NOAA/Environmental Technology Laboratory, Boulder, Colorado

## 1. INTRODUCTION

A midlatitude frontal precipitation system was observed by the Tropical Rainfall Measuring Mission (TRMM) satellite on 19 February 2001 in the Eastern Pacific. Three consecutive overpasses from the TRMM microwave imager (TMI) and the precipitation radar (PR) provide observations of the structure of a narrow cold frontal rainband (NCFR) and a wide cold frontal rainband (WCFR). A Penn State University/National Center for Atmospheric Research mesoscale model (MM5) simulation is used to study the distribution of precipitation within the system. The present study investigates the performance of the Goddard microphysics scheme by comparing observed radar reflectivities and brightness temperatures (TB) with simulated values.

## 2. METHODOLOGY

The PSU-NCAR MM5 model (Version 3.6) is used to conduct a 48-h simulation of the precipitation system from 0000 UTC 18 to 0000 UTC 20 February 2001. The model grids consist of four two-way interactive nested domains. The outermost domain contains 100 × 85 grid points in the *x* and *y* directions with a grid spacing of 45 km. The nested domains contain 148 × 121, 199 × 199, and 448 × 283 grid points with grid spacings of 15, 5, and 1.7 km. Fifty-one vertical sigma levels are used in each domain with 22 levels located below 850 mb. National Center for Environmental Prediction AVN-model analyses with 1° horizontal and 6-h temporal resolution are used to provide the initial and boundary conditions. The outer three domains are initialized at 0000 UTC 18 February and run for 48 hours, while the innermost domain is initialized at 1700 UTC 18 February and run for 22 hours.

Cloud processes in the model include the Grell cumulus parameterization (Grell et al 1995) on the 45- and 15-km domains to account for unresolved convective processes and the Goddard 3-ice phase (cloud ice, snow, and graupel) explicit microphysics parameterization on all grids (Tao and Simpson 1993; Braun and Tao 2000). Boundary layer processes are represented by the Eta PBL scheme, a Mellor-Yamada scheme developed by Janjic (1990, 1994). Longwave and shortwave radiative processes are based on the cloud-radiation scheme of Dudhia (1989). The MM5 simulation from domain 3 (5-km) has been used as input into a cloud-radiative-transfer model to calculate the simulated microwave brightness temperatures.

The normalized polarization (NP) at 19 GHz and the scattering index (SI) at 85 GHz are derived from the brightness temperatures as follows (Petty, 1994):

$$NP=(TB_v-TB_h)/(TB_v-TB_h)_{clear}$$

$$SI=NP\cdot TB_{v,clear}+(1-NP)\cdot 273K-TB_v$$

The subscripts *v* and *h* represent vertical and horizontal polarization, respectively. The subscript *clear* indicates a clear air pixel. For the TRMM data, the clear-air pixel value is estimated from selected rain-free points near the main precipitation band. In the model simulation, the clear-air pixel value is calculated with all the cloud and precipitation hydrometeors excluded.

The NP at 19 GHz (NP19) is approximately equal to the square of transmittance due to cloud and precipitation, also called the attenuation index (0 means a completely opaque rain/cloud region; 1 means a cloud-free ocean scene). The SI at 85 GHz (SI85) represents the effects of scattering due to precipitation ice (Petty, 1994). In this study, NP19 and SI85, as well as the vertically averaged reflectivity, are compared between observations and simulations.

## 3. OBSERVATION AND SIMULATION COMPARISONS

### *a) Rain at 19 GHz*

The vertically averaged reflectivity (mean dBZ) within the lowest 1.5 km above the earth's surface and NP19 are examined to evaluate the performance of the GSFC microphysics scheme against the TRMM observations for liquid precipitation. The mean dBZ is smoothed to match the TMI horizontal resolution at 19 GHz.

Figure 1 shows the 0-1.5 km mean dBZ, NP19, and a scatter plot of the two variables for overpass 18594 at 0023 UTC, 19 February. The PR (Fig.1a) captures the southern side of the leading convective line (namely, the NCFR) and the enhanced precipitation in the trailing stratiform area (namely, the WCFR). With a wider swath from TMI, a broader portion of the frontal rainband is shown in NP19 (Fig. 1b). As expected, the rainy area from the smoothed mean dBZ (contours in Fig. 1b) and NP19 (shading) generally agree with each other. According to the location relative to the front, the scene

*Corresponding author address: Mei Han, NASA GSFC, Code 613.1, Greenbelt, MD 20770; e-mail: han@agnes.gsfc.nasa.gov.

is divided into four sections, including the post-frontal portion, the backside portion, the main-frontal portion, and the leading edge. Figure 1c shows that different portions of the precipitation correspond to different clusters of data points in the scatter plot. The precipitation in the post-frontal and backside portions is associated with light scattered showers, which produce a lower attenuation effect. The main-frontal rainband consists of the intense NCFR and the WCFR, contributing to strong attenuation. The precipitation at the leading edge of the rainband is also weak. However, it shows a stronger attenuation effect than that in the post-frontal region. One possible cause of this difference may be the strong contrast of the background temperature and moisture between the airs ahead and behind the front. Another factor may be the choice of the clear-air values of $(TB_v\text{-}TB_h)_{clear}$. Analyses from the other two overpasses show similar results and are not discussed here.

Figure 2 shows the simulated 0-1.5 km mean dBZ, NP19, and the scatter plot of the two variables at 0200 UTC 19 Feb. The simulated reflectivity captures the main features of the NCFR and WCFR, as well as post-frontal and pre-frontal showers. The domain is divided into three sections, including post-frontal, main-frontal, and pre-frontal, portions in a manner slightly different to the TRMM observations. The smoothed mean dBZ and the NP19 show good correspondence (Fig. 2b). The data points from the different portions also tend to lie in different clusters (Fig. 2c). The simulated post-frontal rain showers are very intense, and therefore some of the post-frontal data points show quite strong attenuation, differing from the TRMM observations. The main-frontal rainband mostly consists of data points with high reflectivity and strong attenuation, comparable to the TRMM data. The simulated pre-frontal rain showers have light reflectivities with weak attenuation, although somewhat stronger than in the post-frontal region for a given reflectivity. However, this portion does not directly compare to the TRMM leading-edge region since the TRMM observations correspond to the high gradient region at the leading edge of the NCFR while the model information corresponds to a region of widespread pre-frontal showers.

Figure 3 shows the relationship of the 0-1.5 km mean dBZ and NP19 from the three TRMM overpasses and the model simulation. Figure 3a shows data from the entire model domain while Fig. 3b excludes the post-frontal region. The figure suggests that the model simulation matches the observations reasonably well for the liquid precipitation, except within the post-frontal region where the simulated reflectivities are too high.

***b) Precipitation ice at 85 GHz***

To examine the performance of the microphysics scheme for the ice phase, the reflectivity is averaged within the 3-5 km layer, above the freezing level. The scattering index, SI85, is calculated and compared with the mean dBZ. The horizontal resolution of TMI at 85 GHz is ~5 km, about the same as that of the PR.

Figure 4 shows the 3-5 km mean dBZ, SI85, and the scatter plot of the two variables for overpass 18594. The mean reflectivity in the ice layer is very intense along the NCFR with a broad region of weaker reflectivity associated with the WCFR (Fig. 4a). The SI85 field (Fig. 4b) agrees reasonably well with the 3-5 km mean reflectivity. With the high horizontal resolution at 85 GHz, the scattering signatures of the NCFR and WCFR can be readily differentiated. As with the analysis for the rain layer, the scene is divided into four sections. The data points in the main-frontal rainband are characterized by high mean reflectivity and strong scattering, with the highest dBZ and strongest SI85 value corresponding to the NCFR (Fig. 4c). Below 27 dBZ, a close relationship between the mean dBZ and SI85 is found. Above 27 dBZ, the data points are quite scattered, with SI85 ranging from 10 to 90. This result may be indicative of strongly varying characteristics of the ice, e.g., graupel, such as variations in density and particle size distributions. In addition, these data points lie mainly within the NCFR. Since the NCFR is as narrow as ~5-10 km in width, it is possible that the scanning geometry of the PR and TMI might also contribute to such scatter. Further study is needed to confirm the above tentative explanations.

The model simulated mean dBZ and SI85 are shown in Fig. 5. The structure of the simulated precipitation ice generally agrees with the TRMM observations, but with some important differences. The maximum magnitude of the mean reflectivity within the main-frontal band is ~5 dBZ less than in the TRMM observations. In addition, the post-frontal precipitation ice is very intense with very strong scattering effects. The scatter plot of dBZ versus SI85 shows a close relationship at all reflectivity values, with peak reflectivities and SI85 values much higher than in the TRMM observations (Fig. 4c). The lack of scatter at higher reflectivities may be due to the very constrained properties of graupel in the model (constant density, fixed intercept parameter of the assumed Marshall-Palmer size distribution).

Different forms of precipitation ice have different scattering characteristics; for example, graupel is a more effective scatterer than snow. In the simulation, the ratio of graupel to total precipitation ice (graupel and snow) within the 3-5km layer is investigated (Fig. 6). A good portion of the main-frontal rainband has a graupel ratio greater than 50%. Some intense showers in the post-frontal region consist of graupel ratios greater than 70% (Fig. 6a). Figure 6b shows that the scattering effect dramatically increases as the reflectivity increases, and above 27 dBZ, the graupel ratio exceeds 50%. Comparison between Figs. 6b and 5c confirms the domination of graupel in the main-frontal rainband region, and also highlights the extremely strong scattering effect associated with high graupel concentrations in the post-frontal showers.

Data points from two TRMM overpasses are compared with the simulation in Fig. 7. The simulation generally produces higher reflectivities and scattering than is observed by TRMM. The simulated post-frontal precipitation, in particular, contributes too much ice and

scattering, which is one of the main discrepancies between the TRMM observations and the model simulation. The observations and simulation agree much better when the post-frontal precipitation is excluded (Fig. 7b). Below 27 dBZ, where a tight relationship between the mean dBZ and SI85 is found in the TRMM observations, the observations agree well with the simulation, particularly points with low graupel ratios. Above 27 dBZ, the majority of the simulated data points occur in the high graupel-ratio category. They also show a close relationship between the mean dBZ and SI85, in contrast with the more scattered data points from TRMM. As mentioned above, this discrepancy between the simulation and the TRMM observations may indicate that the model parameters for graupel (e.g., density, intercept parameter) are too restricted and cannot represent the variability of these characteristics that occur in nature.

## 4. SUMMARY AND FUTURE WORK

The model simulation agrees well with the TRMM observations for liquid precipitation, with layer mean reflectivities and normalized polarization values in good agreement, except in the post-frontal region where simulated showers are more intense than observed. However, the simulation produces more graupel than the observations suggest. New simulations with a modified GSFC microphysics scheme will be tested with the aim of improving the simulation of graupel and snow, as well as their scattering effects.

In addition, new methods for calculating NP19 will be tested to determine the extent to which the clear-sky information contributes to the apparent clustering in the scatter plot of the mean dBZ vs. NP19 for the TRMM observations. Using the cloud-radiative-transfer model, the influence of the variation of the graupel densities on the scattering effect will also be examined.

ACKNOWLEDGEMENTS

This work was supported by Dr. Ramesh Kakar at NASA Headquarters with funds from the NASA Precipitation Measurement Mission Science program.

REFERENCES

Braun, S. A., and Tao W.-K., 2000: Sensitivity of high-resolution simulations of Hurricane Bob (1991) to planetary boundary layer parameterizations. *Mon. Wea. Rev.,* **128,** 3941-3961.

Dudhia, J., 1989: Numerical study of convection observed during the winter monsoon experiment using a mesoscale two-dimensional model. *J. Atmos. Sci.,* **46,** 3077-3107.

Grell, G. A., J. Dudhia, and D. R. Stauffer, 1995: A description of the fifth-generation Penn State/NCAR Mesoscale Model (MM5). *NCAR Tech. Note TN-398+STR,* 122pp.

Janjic, Z. I., 1990: The step-mountain coordinate: Physical package. *Mon. Wea. Rev.,* **118,** 1429–1443.

____, 1994: The step-mountain eta coordinate model: Further development of the convection, viscous sublayer, and turbulent closure schemes. *Mon. Wea. Rev.,* **122,** 927–945.

Petty, G. W., 1994: Physical retrievals of over-ocean rain rate from multichannel microwave imagery. Part I: The theoretical characteristics of normalized polarization and scattering indices. *Meteorol. Atmos. Phys.,* **54,** 79-99.

Tao, W.-K. and J. Simpson, 1993: The Goddard Cumulus Ensemble Model. Part I: Model description. *Terr. Atmos. Oceanic Sci.,* **4,** 35-72.

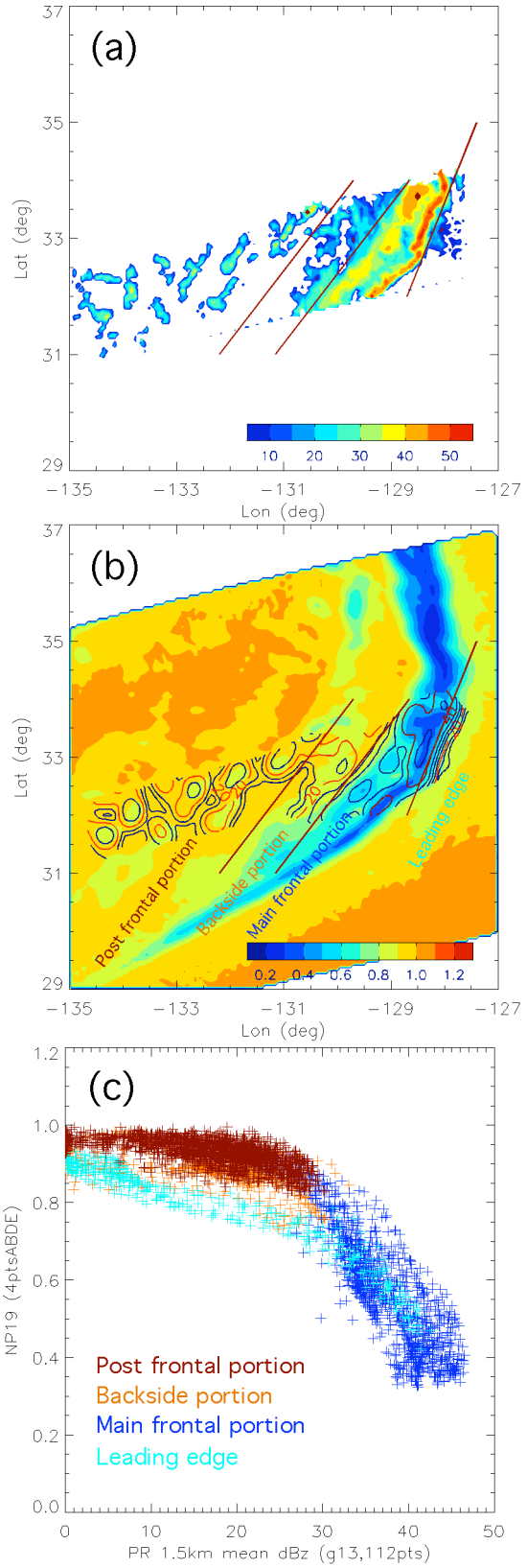


FIG. 1. TRMM observations from overpass 18594 at 0023 UTC, 19 Feb, 2001. (a) 0-1.5 km mean dBZ; (b) NP19 (shaded) and the smoothed mean dBZ (Contours starts at 10 dBZ with 5 dBZ intervals. The 20 and 40 dBZ contours are labeled and colored in orange.); (c) scatter plot of the two variables in (b), colored for different sections. Red lines in (a) and (b) divide the domain into 4 sections.

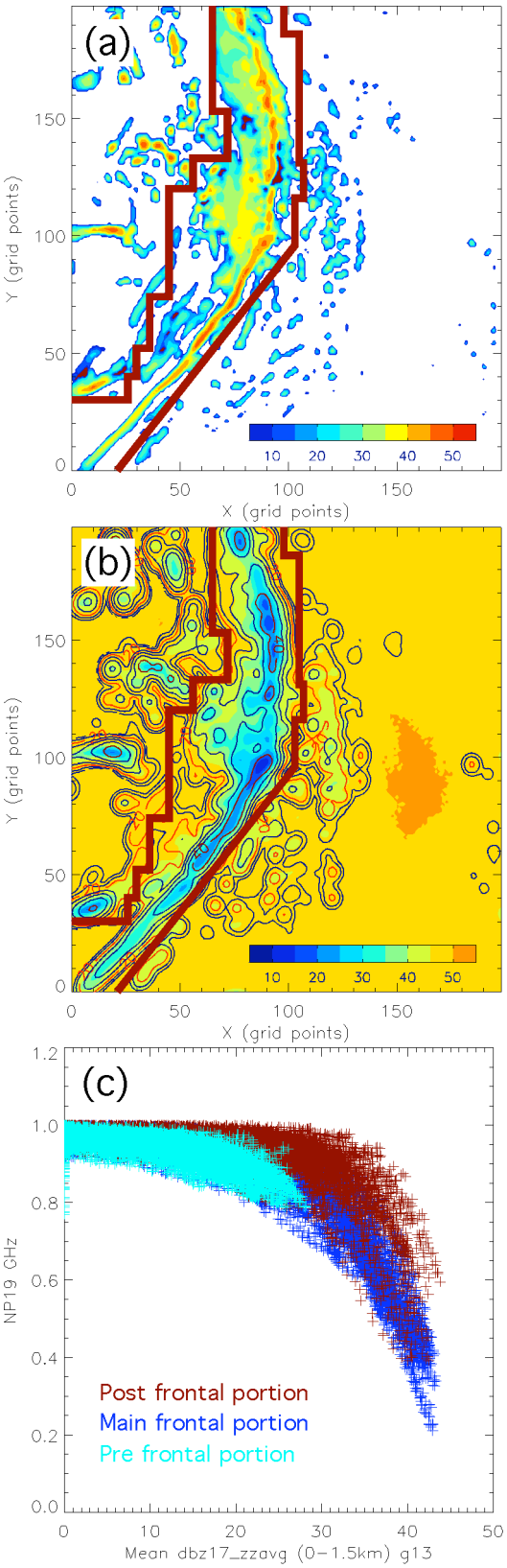


FIG. 2. Model simulation at 0200 UTC, 19 Feb, 2001. (a) and (b) are the same as FIG. 1, except the bold red lines divide the domain into 3 sections. (c) scatter plot of the two variables in (b), colored for different sections.

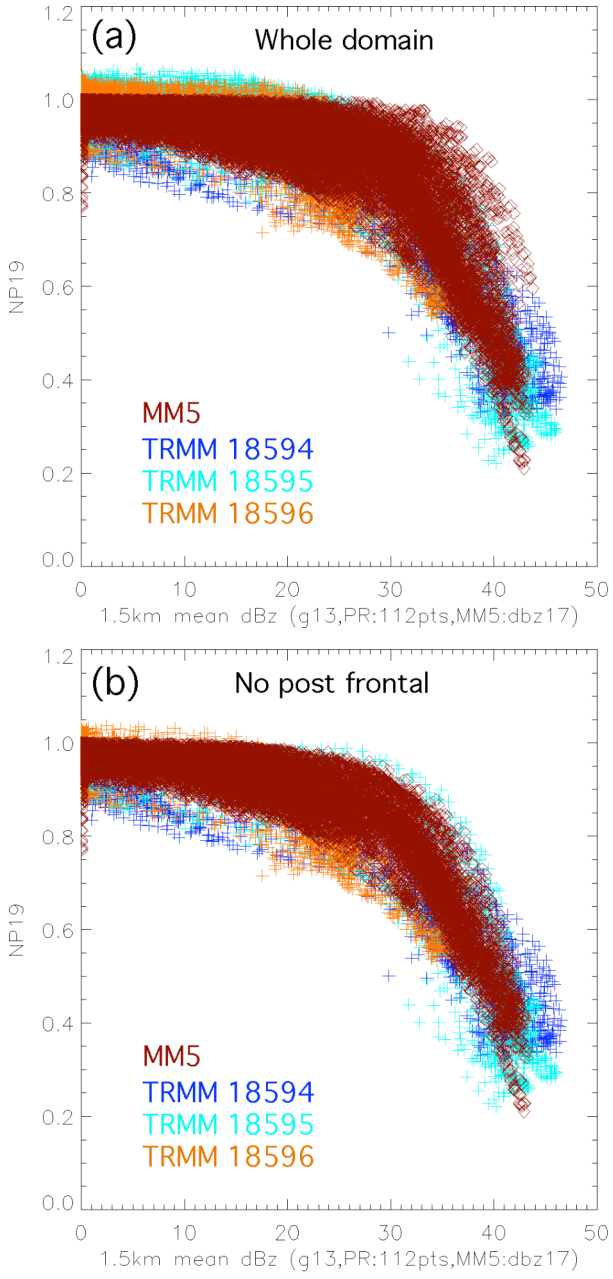


FIG. 3. Observed and simulated 0-1.5 km mean dBZ vs. NP19. Three TRMM overpasses, 18594, 18595, and 18596 are shown with crosses. The model simulation at 0200 UTC 19 Feb. is shown with red diamonds. (a) Whole domain (b) Same as (a), except the post-frontal portion is eliminated.

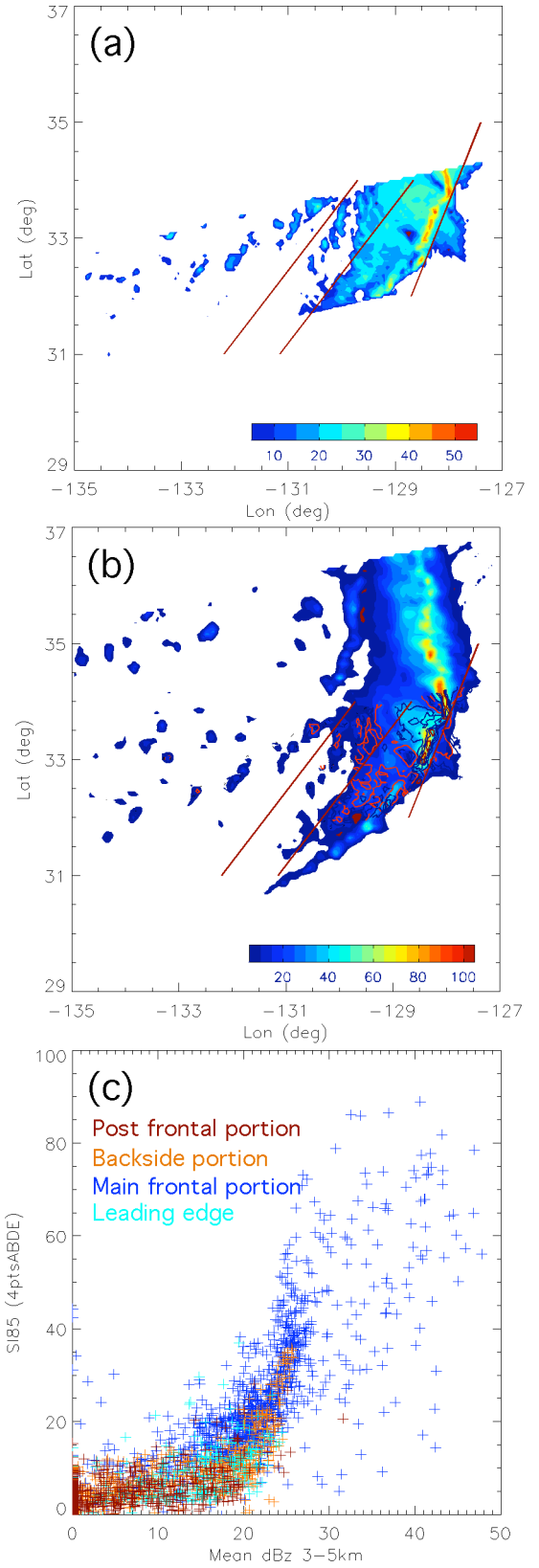


FIG. 4. Same as FIG. 1, except for precipitation ice. (a) 3-5 km mean dBZ; (b) SI85 (shaded) and the 3-5 km mean dBZ (contoured); (c) scatter plot of the two variables in (b).

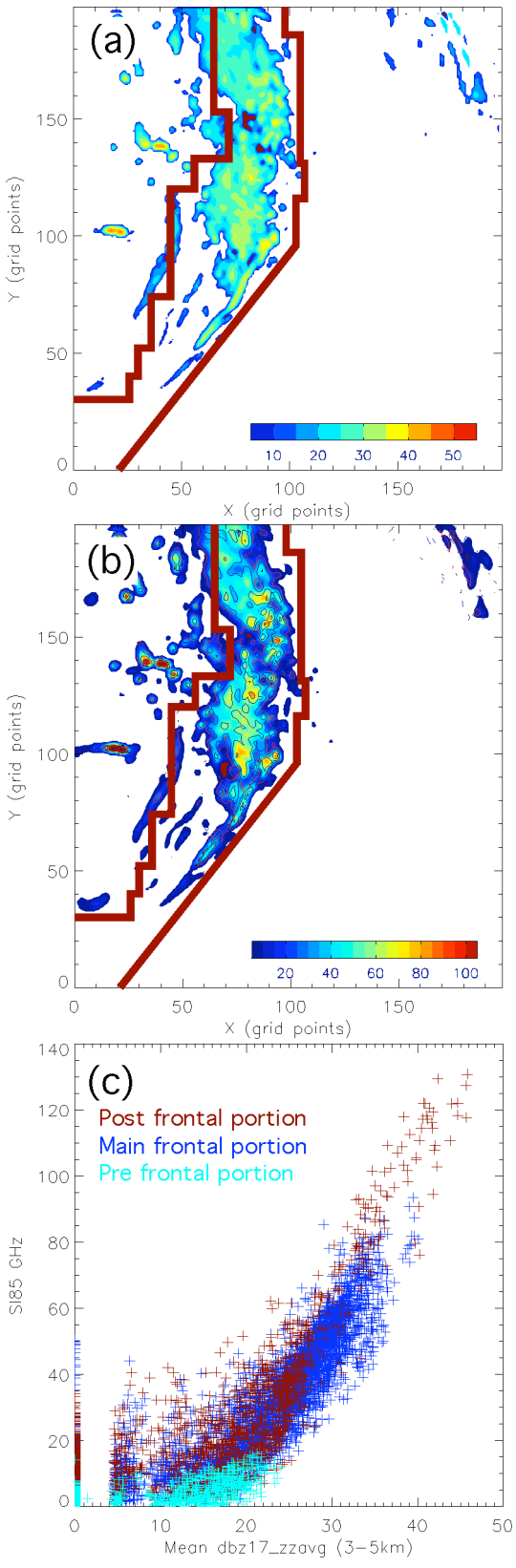


FIG. 5. Same as FIG. 2, except for precipitation ice. (a) 3-5 km mean dBZ; (b) SI85 (shaded) and the 3-5 km mean dBZ (contoured); (c) scatter plot of the two variables in (b).

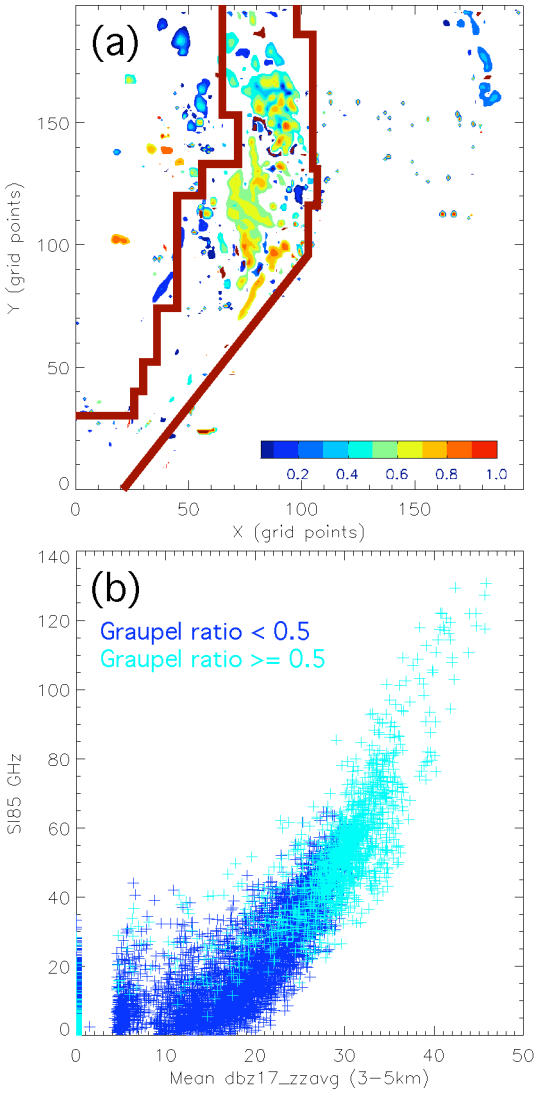


FIG. 6. (a) The ratio of graupel to total precipitation ice (graupel and snow) within 3-5 km layer; (b) 3-5 km mean dBZ vs. SI85 (blue: graupel ratio < 0.5; cyan: graupel ratio >= 0.5).

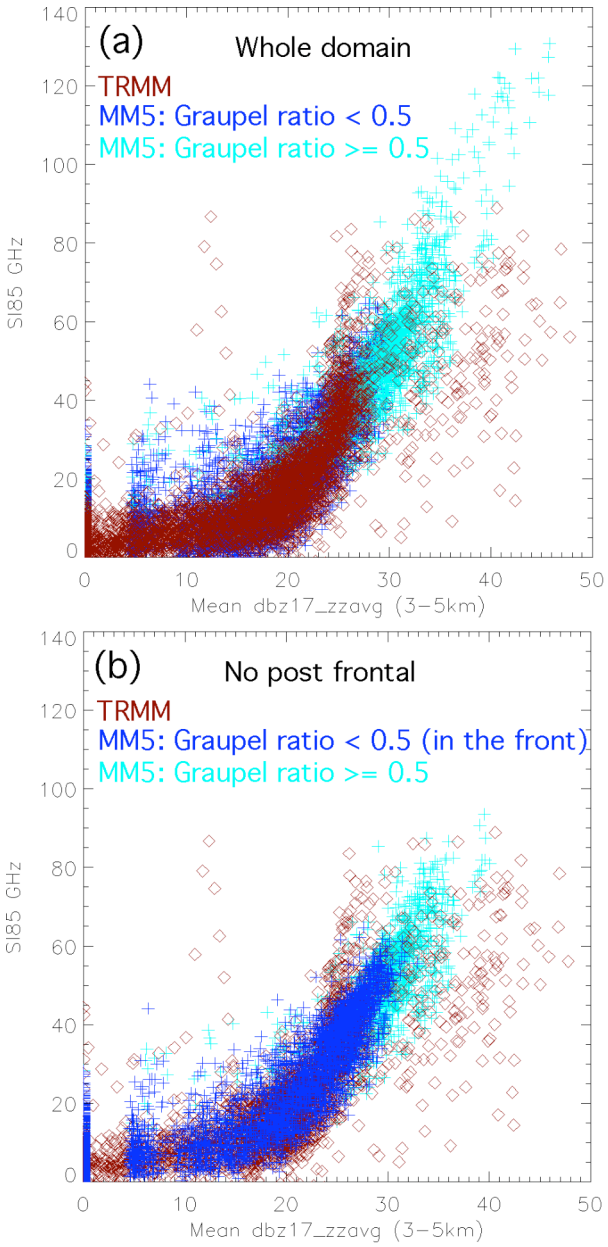


FIG. 7. Observed and simulated 3-5 km mean dBZ vs. SI85. Two TRMM overpasses, 18594 and 18595, are shown in red diamonds. The model simulation at 0200 UTC 19 Feb. is shown in blue (graupel ratio < 0.5) and cyan (graupel ratio >= 0.5) crosses. (a) Whole domain (b) Same as (a), except the post-frontal portion is eliminated. The low graupel ratio part (blue) is brought to front in (b) for comparison, see text.